PAPER • OPEN ACCESS

Abnormal quantum moment of inertia and structural properties of electrons in 2D and 3D quantum dots: an *ab initio* path-integral Monte Carlo study

To cite this article: Tobias Dornheim and Yangqian Yan 2022 *New J. Phys.* **24** 113024

View the article online for updates and enhancements.

New Journal of Physics

The open access journal at the forefront of physics

PAPER

Abnormal quantum moment of inertia and structural properties of electrons in 2D and 3D quantum dots: an *ab initio* path-integral Monte Carlo study

Tobias Dornheim[1,2,*] and **Yangqian Yan**[3,4]

1   Center for Advanced Systems Understanding (CASUS), 03581 Görlitz, Germany
2   Helmholtz-Zentrum Dresden-Rossendorf (HZDR), 01328 Dresden, Germany
3   Department of Physics, The Chinese University of Hong Kong, Hong Kong, People's Republic of China
4   The Chinese University of Hong Kong Shenzhen Research Institute, Shenzhen, People's Republic of China
*   Author to whom any correspondence should be addressed.

E-mail: t.dornheim@hzdr.de

Abstract

We present extensive new direct path-integral Monte Carlo results for electrons in quantum dots in two and three dimensions. This allows us to investigate the nonclassical rotational inertia (NCRI) of the system, and we find an abnormal negative quantum moment of inertia (2014 *Phys. Rev. Lett.* **112** 235301) under some conditions. In addition, we study the structural properties by computing a re-normalized, angular-resolved center-two particle correlation function. Remarkably, we find no connection between the spatial structure and the NCRI, since the former can be nearly identical for Fermi- and Bose-statistics for parameters where the superfluid fraction is diverging towards negative infinity.

1. Introduction

The study of fermionic many-body systems at finite temperature constitutes a highly active field of research, offering a plethora of interesting physical effects. Prominent examples include quantum liquids such as ultracold ^{3}He [1–5], which undergoes a pairing-induced superfluid phase transition at low temperature [6] and exhibits an intriguing, non-trivial phonon-roton-maxon dispersion relation in the spectrum of collective excitations [3–5]. A second relevant example is given by exotic *warm dense matter* [7–11], which naturally occurs in astrophysical objects like brown dwarfs [12, 13] and giant planet interiors [14, 15], and has been predicted to manifest on the pathway towards inertial confinement fusion [16].

A particularly interesting system is given by electrons in quantum dots [17], which are studied in the present work. First and foremost, we mention that these exhibit a number of interesting physics, like the quantum breathing mode response to a monopole excitation [18, 19], and the formation of Wigner molecules [20] and even crystallization [21] at strong coupling. A further important research topic regarding electrons in quantum dots is the investigation of addition energies [22–24], which can be directly compared to experimental measurements [25]. Moreover, we mention the formation of vortices and their dependence on the respective spatial structure [26, 27], and the rich interplay of the rotational inertia with a strong external magnetic field [28].

From a theoretical perspective, the accurate description of all aforementioned systems requires to simultaneously take into account (i) coupling effects due to the interactions, (ii) thermal excitations as a result of the finite temperature, and (iii) quantum degeneracy effects like Pauli blocking since identical fermions are indistinguishable. In addition, confined few-body systems [29] additionally require to take into account the interplay between (i)–(iii) and (iv) the external potential, which, in the present study, is modelled as a harmonic oscillator. Due to these challenges, electrons in quantum dots constitute a rigorous benchmark that is often used to test novel many-body methods, e.g., references [30–39].

In the present work, we use the direct path-integral Monte Carlo (PIMC) method [40, 41] without any nodal constraints [42] to simulate electrons in both 2D and 3D harmonic confinements. Therefore, our simulations are afflicted with the notorious fermion sign problem (FSP) [43–45] (in practice, we spend up to $\mathcal{O}(10^4)$ CPUh for a single calculation), but are exact within the given Monte Carlo error bars, which allows for a rigorous treatment of the intriguing interplay between the effects (i)–(iv) mentioned above. All PIMC results are available online [46] and can be used e.g. to test new methods and approximations. From a practical perspective, the PIMC method gives us direct access to the quantum moment of inertia—often characterized in terms of the so-called superfluid fraction—of the system [47, 48], which exhibits a remarkable abnormal divergence towards negative infinity in the case of fermions for some conditions [49, 50]. This effect was first reported by Yan and Blume [49] for a short-range pair potential and subsequently found by Dornheim [50] for quantum-dipole systems, and has been explained in terms of the symmetry of the thermal density matrix. Here, we extend these considerations to electrons in quantum dots and find analogous behaviour. In addition, we study the structural properties of the system using a renormalised, angular-resolved center-two particle (C2P) correlation function [51], which efficiently takes into account the rotational symmetry of the system. This allows us to resolve the interesting interplay between quantum statistics and the Coulomb interaction between pairs of electrons, and to explore the connection between the aforementioned abnormal superfluid fraction and the static structure.

The paper is organized as follows: in section 2, we introduce the relevant theoretical background including the model system (1), the utilized PIMC simulation approach section 2.2, the estimation of the nonclassical rotational inertia (NCRI) in terms of the superfluid fraction section 2.3, and finally the C2P correlation function section 2.4. Section 3 is devoted to the presentation of our extensive new simulation results, which we start by shortly revisiting the noninteracting system in section 3.1. Subsequently, we study both the quantum moment of inertia and the structural properties of electrons in quantum dots, focusing on the dependence on the temperature section 3.2, on the system-size section 3.3, and on the coupling strength section 3.4. The paper is concluded with a concise summary and outlook in section 4.

2. Theory

2.1. Model system

We consider N spin-polarized electrons in both two- and three-dimensional quantum dots, which we model by a simple harmonic potential [17]. This gives the Hamiltonian

$$\hat{H} = -\frac{1}{2}\sum_{k=1}^{N}\nabla_k^2 + \frac{1}{2}\sum_{k=1}^{N}\hat{\mathbf{r}}_k^2 + \sum_{k>l}^{N}\frac{\lambda}{|\hat{\mathbf{r}}_l - \hat{\mathbf{r}}_k|}, \tag{1}$$

where we assume oscillator units, corresponding to the characteristic length $l_0 = \sqrt{\hbar/m\Omega}$ (with Ω being the trap frequency) and energy scale $E_0 = \hbar\Omega$. The first term corresponds to the kinetic contribution $\hat{K}$ and the last two terms to the external potential and the Coulomb interaction, $\hat{V}_{\mathrm{ext}}$ and $\hat{W}$, respectively. Moreover, the coupling constant λ can, in principle, be tuned in experiments [52].

2.2. Path-integral Monte Carlo

We use the direct PIMC method [53, 54], see reference [40] for an extensive review article. In a nutshell, the basic idea behind PIMC is to stochastically sample the thermal density matrix in the canonical ensemble

$$\rho(\mathbf{R}_1, \mathbf{R}_2, \beta) = \langle\mathbf{R}_1|e^{-\beta\hat{H}}|\mathbf{R}_2\rangle, \tag{2}$$

where $\hat{H}$ is the Hamiltonian, $\beta = 1/k_{\mathrm{B}}T$ the inverse temperature, and $\mathbf{R} = (\mathbf{r}_1, \ldots, \mathbf{r}_N)^{\mathrm{T}}$ contains the coordinates of all N particles. While a direct evaluation of equation (2) is not possible as different contributions to the full Hamiltonian do not commute, one makes use of a Trotter decomposition [55] into P terms that are each given at P-times the original temperature. The resulting scheme becomes exact in the limit of large P and the respective convergence has been carefully checked; see reference [56] for a detailed discussion of different factorization schemes. The PIMC method thus allows for the quasi-exact evaluation of thermal expectation values

$$\langle\hat{A}\rangle = \mathrm{Tr}\left(e^{-\beta\hat{H}}\hat{A}\right) \tag{3}$$

within the given Monte Carlo error bar, which scales as $\Delta A \sim 1/\sqrt{N_{\mathrm{MC}}}$ with the number of Monte Carlo samples N_{MC}. In practice, we use a canonical adaption [57] of the worm algorithm presented by Boninsegni *et al* [58, 59].

An additional obstacle regarding the PIMC simulations of fermions (i.e., particles obeying Fermi–Dirac statistics such as electrons or protons) is given by the anti-symmetry of equation (2) under the exchange of

particle coordinates [41]. First and foremost, negative terms cannot be interpreted as a probability distribution, and the expectation value from equation (3) gets modified to [45]

$$\langle \hat{A} \rangle = \frac{\langle \hat{A}\hat{S} \rangle'}{\langle \hat{S} \rangle'}, \tag{4}$$

where $\langle \ldots \rangle'$ denotes the expectation value computed from the absolute values of the density matrix, and $\hat{S}$ measures the respective sign. In particular, the denominator of equation (2) is called the *average sign S* and constitutes a straightforward measure for the amount of cancellation within the fermionic PIMC simulation. This can easily be seen by considering the first-order term to the relative statistical uncertainty [60],

$$\frac{\Delta A}{A} \sim \frac{1}{S\sqrt{N_{\mathrm{MC}}}}, \tag{5}$$

which directly implies that the Monte Carlo error bar increases when the average sign S gets small. In fact, S exponentially decreases both with the inverse temperature β and the system size N, which can be directly translated to ΔA as

$$\frac{\Delta A}{A} \sim \frac{e^{\beta N \Delta f}}{\sqrt{N_{\mathrm{MC}}}}, \tag{6}$$

where Δf denotes the difference in the free energy density of the original $(\langle \ldots \rangle)$ and the modified $(\langle \ldots \rangle')$ systems. Equation (6) is the root of the infamous FSP [45], as the exponential increase of $\langle A \rangle$ can only be compensated by increasing the compute time as $1/\sqrt{N_{\mathrm{MC}}}$, which quickly becomes infeasible. In fact, equation (6) constitutes the central computational bottleneck in our simulations and limits the feasible system size to $N \leqslant 10$.

2.3. Nonclassical rotational inertia

Throughout the relevant literature [48–50, 52], the NCRI of a quantum system is characterized in terms of the so-called *superfluid fraction*. In an actual superfluid [61], it is physically intuitive to use the Landau two-fluid model, where the total density is decomposed into a *normal* part reacting to a rotation of the system, and a *superfluid* part that remains unaffected,

$$n = n_{\mathrm{n}} + n_{\mathrm{sf}}. \tag{7}$$

The corresponding *superfluid fraction* is then defined as the ratio of the superfluid to the total density,

$$\gamma_{\mathrm{sf}} = \frac{n_{\mathrm{sf}}}{n} = 1 - \frac{I}{I_{\mathrm{cl}}}, \tag{8}$$

with I and I_{cl} denoting the actual (i.e., quantum) and classical moments of inertia. Within the path-integral picture, the former can be straightforwardly estimated as [61]
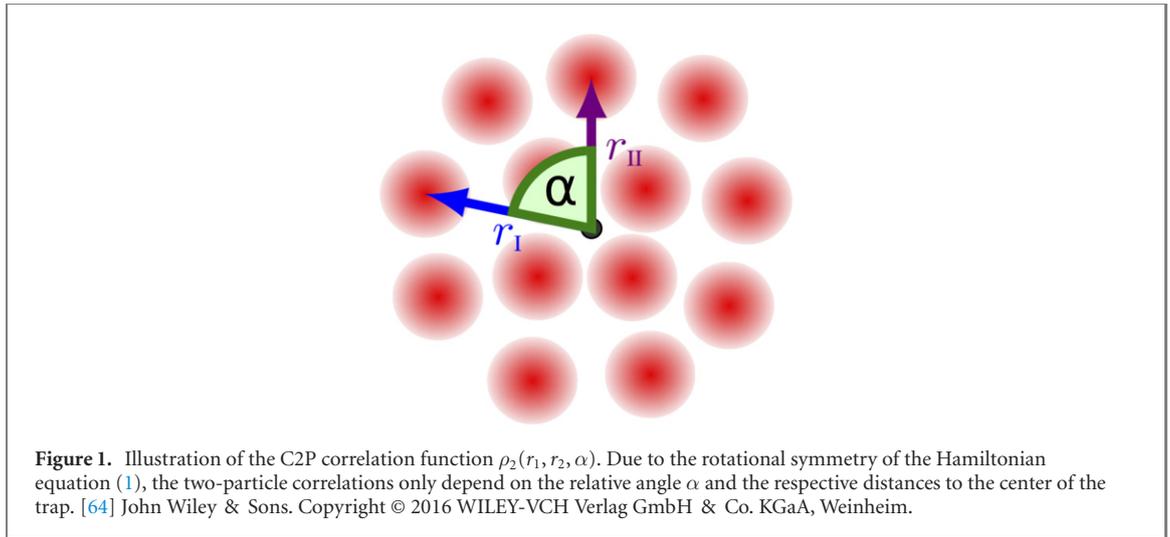
$$\gamma_{\mathrm{sf}} = \frac{4m^2 \langle A_z^2 \rangle}{\beta \hbar^2 I_{\mathrm{cl}}}, \tag{9}$$

which is often being referred to as the area estimator in the respective literature. In particular, equation (9) depends on the area that is enclosed by the paths in the plane perpendicular to the rotational axis,

$$\mathbf{A} = \frac{1}{2} \sum_{k=1}^{N} \sum_{i=1}^{P} \left(\mathbf{r}_{k,i} \times \mathbf{r}_{k,i+1} \right), \tag{10}$$

with $\mathbf{r}_{k,i}$ being the coordinate of particle k on the imaginary-time slice i. For completeness, we note that for an ideal (i.e., noninteracting) system, γ_{sf} can be computed semi-analytically [49, 62], see reference [50] for the corresponding formulas.

Within the context of the present work, equation (8) constitutes a straightforward measure of the impact of quantum effects onto the moment of inertia. In particular, it is easy to see that it holds $\gamma_{\mathrm{sf}} = 0$ in the classical limit where, by definition, it is $I = I_{\mathrm{cl}}$. Regarding the evaluation of γ_{sf} via the area estimator given in equation (9), this limit is straightforwardly recovered as the area enclosed by the paths vanishes in the case of point particles. One possible manifestation of quantum effects onto the moment of inertia is to make it smaller, which is the standard case for Bose systems. This is indicated by $\gamma_{\mathrm{sf}} > 0$ with the limit of γ_{sf} implying a completely vanishing I. On the other hand, Yan and Blume [49] have pointed out that, remarkably, quantum effects can actually increase the moment of inertia in certain confined Fermi systems; this is reflected by $\gamma_{\mathrm{sf}} < 0$. A negatively diverging superfluid fraction is thus the consequence of a diverging quantum moment of inertia.

Figure 1. Illustration of the C2P correlation function $\rho_2(r_1, r_2, \alpha)$. Due to the rotational symmetry of the Hamiltonian equation (1), the two-particle correlations only depend on the relative angle α and the respective distances to the center of the trap. [64] John Wiley & Sons. Copyright © 2016 WILEY-VCH Verlag GmbH & Co. KGaA, Weinheim.

Let us conclude this discussion of NCRI by re-iterating our earlier point that a non-zero superfluid fraction as it is defined in equation (9) does not necessarily indicate the usual phenomenon of superfluidity that manifests for example as a frictionless flow in ultracold ^{4}He [40]. In fact, superfluidity naturally emerges as a long-range order in the off-diagonal density matrix [63], which is not possible for the small system sizes considered in this work. Therefore, one should interpret it strictly in terms of NCRI, i.e., as a quantum effect on the moment of inertia, as it has been introduced above. Still, since the concept and definition of the *superfluid fraction* are well-known from previous studies [48–50, 52, 61], we will stick to it throughout this work as well.

2.4. Structural properties

The second central aim of the present work is the investigation of the impact of quantum statistics on the structural properties of electrons in quantum dots. To this end, we have implemented the renormalized, angular-resolved C2P correlation function [51], which has already been successfully applied to harmonically confined quantum systems in earlier works [50, 64, 65]. Indeed, such reduced correlation functions constitute a well-known tool for the investigation of finite systems [51, 66, 67]. The basic idea is illustrated in figure 1, which shows an exemplary configuration of $N = 13$ particles in a 2D harmonic trap. Here the shaded red circles illustrate the quantum smearing of the electrons, distinguishing them from classical point particles. To characterize two-particle correlations, one can make use of the rotational symmetry of the problem and use the modified coordinates (distance to the center of the trap of particles I and II, and the angle α between them) shown in figure 1 without any loss of information. More specifically, we estimate the corresponding two-particle density matrix $\rho_2(r_1, r_{II}, \alpha)$ as a histogram in our PIMC simulation.

In addition, Thomsen and Bonitz [51] have suggested that it would be advantageous to filter out effects that are caused by the inhomogeneous density profile $n(r)$ and not by correlation effects themselves. To this end, the actual C2P is normalized by the two-particle density matrix of a hypothetical uncorrelated system with the same radial density profile as the interacting one,

$$\rho_2^0(r_1, r_{II}, \alpha) = \frac{N-1}{N} 4\pi r_1 r_{II} n(r_1) n(r_{II}), \tag{11}$$

and is thus given by
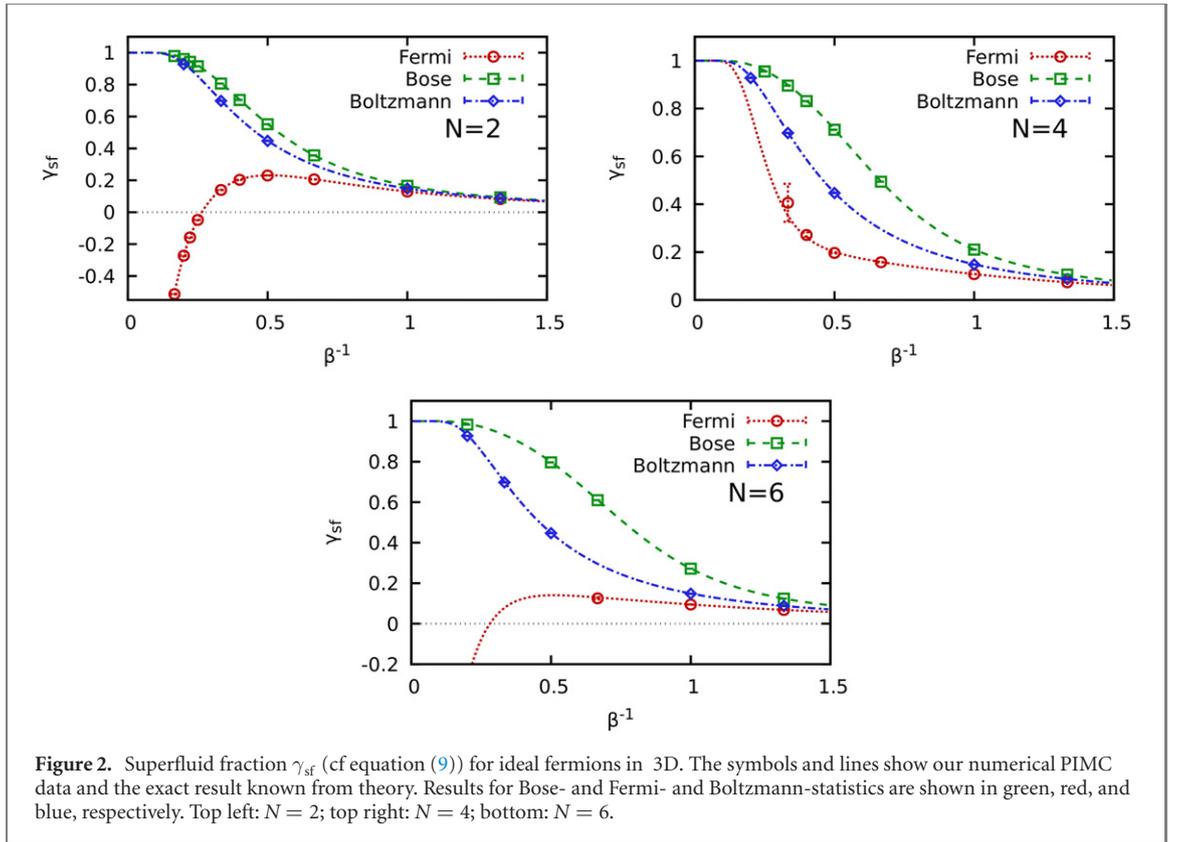
$$g_{c2p}(r_1, r_{II}, \alpha) = \frac{\rho_2(r_1, r_{II}, \alpha)}{\rho_2^0(r_1, r_{II}, \alpha)}. \tag{12}$$

We note that equation (11) does not depend on the angle α by design, as noninteracting particles are not affected by their relative orientation towards each other.

While the C2P defined in equation (12) already constitutes a sophisticated tool for the investigation of spatial correlations, the visualization and analysis of a 3D quantity is often difficult. As a final step, we therefore define the integrated C2P

$$g_{c2p}^{int}(r_1, \alpha; r_{II,min}, r_{II,max}) = \frac{\int_{r_{II,min}}^{r_{II,max}} dr_{II} \rho_2(r_1, r_{II}, \alpha)}{\int_{r_{II,min}}^{r_{II,max}} dr_{II} \rho_2^0(r_1, r_{II}, \alpha)}, \tag{13}$$

which can be interpreted in the following way: equation (13) constitutes a measure for the probability to find one particle at distance r_1 to the center of the trap, with an angular difference of α to a second particle

Figure 2. Superfluid fraction γ_{sf} (cf equation (9)) for ideal fermions in 3D. The symbols and lines show our numerical PIMC data and the exact result known from theory. Results for Bose- and Fermi- and Boltzmann-statistics are shown in green, red, and blue, respectively. Top left: $N = 2$; top right: $N = 4$; bottom: $N = 6$.

somewhere in the interval $r_{\text{II,min}} \leqslant r_{\text{II}} \leqslant r_{\text{II,max}}$, where the min and max values are typically chosen as the limits of a shell in the density profile $n(r)$.

All results for the C2P shown in this work have been obtained according to equation (13).

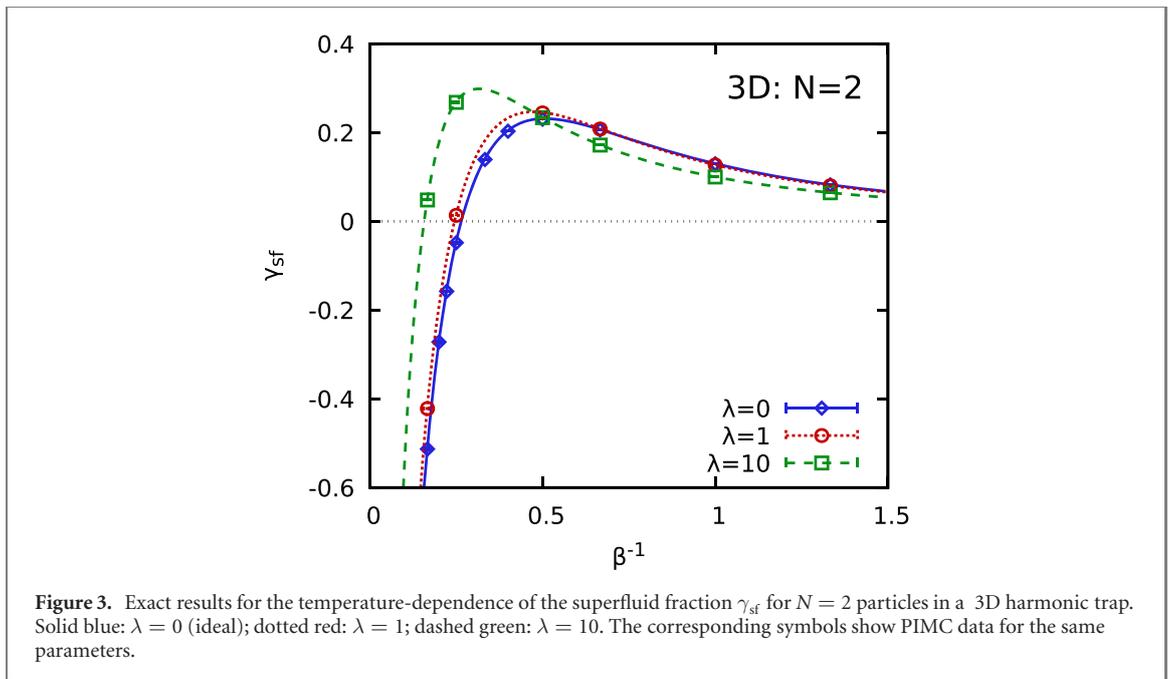## 3. Results

3.1. Noninteracting system

Let us start the discussion of our new simulation results with a brief study of the temperature dependence of the superfluid fraction of noninteracting particles in a 3D harmonic trap. While similar analyses have been presented in 2D in reference [50] and in 3D in reference [49], here we select somewhat different parameters. In addition, the availability of exact analytical results makes it a valuable test case to verify the implementation of our simulation scheme. Finally, the abnormal superfluid fraction of interacting electrons presented in a later section follows the same basic mechanism as the ideal case, which makes it a good starting point.

In figure 2, we show results for $N = 2$ (top left), $N = 4$ (top right), and $N = 6$ (bottom) ideal bosons (green), fermions (red), and distinguishable so-called boltzmannons (blue) with the symbols and lines showing PIMC data and the exact theoretical results. For all three system sizes, the superfluid fraction is small and almost equal for bosons, fermions, and boltzmannons for large temperatures $T = \beta^{-1}$, whereas differences emerge for smaller T. In fact, it always holds

$$\lim_{T \to \infty} \gamma_{\text{sf}} = 0, \tag{14}$$

as the systems becomes purely classical in this limit, $I \to I_{\text{cl}}$. Moreover, we note that the Boltzmann results do, by definition, not depend on the system size N as ideal boltzmannons are fully uncorrelated. The first correction to I_{cl} is due to the finite extension $\lambda_\beta = \sqrt{2\pi\beta}$ of quantum particles, which is similar for all types of quantum statistics. With decreasing temperature, the paths of different particles in a PIMC simulation start to overlap, and the formation of permutation cycles, i.e., paths containing more than a single particle in them, becomes increasingly likely; see reference [41] for a recent extensive discussion. In practice, this leads to an increased impact of quantum statistics, which explains the stark qualitative and quantitative differences between the red, green, and blue data sets.

More specifically, bosons (and also boltzmannons) always attain a superfluid fraction of one in the limit of $T = 0$ at these conditions, independent of the particle number N. Yet, we stress that this does certainly

Figure 3. Exact results for the temperature-dependence of the superfluid fraction γ_{sf} for $N = 2$ particles in a 3D harmonic trap. Solid blue: $\lambda = 0$ (ideal); dotted red: $\lambda = 1$; dashed green: $\lambda = 10$. The corresponding symbols show PIMC data for the same parameters.

not mean that ideal bosons become an actual superfluid, as the Landau criterion requires a small value of the coupling parameter λ in this case [68]. Fermions, on the other hand, exhibit a substantially more complicated behaviour. In particular, the superfluid fraction diverges towards negative infinity for both $N = 2$ and $N = 6$, and attains one for $N = 4$, although for lower temperatures compares to bosons. This remarkable effect has been explained by Yan and Blume [49] in terms of the structure of the density matrix. Specifically, it is the presence of an energetically low-lying state with a finite circulation for some N that leads to a diverging moment of inertia and to the observed behaviour in γ_{sf}.

Finally, we stress the excellent agreement between theory and PIMC data for bosons, fermions, and boltzmannons everywhere, which is a strong verification of our implementation and analysis. In addition, we note that simulations are restricted to above a minimum temperature in the case of fermions due to the FSP (see section 2.2 above), as can be seen most clearly for the leftmost red data point for $N = 4$. In contrast, there is no such issue for bosons, where simulations are possible even at extremely low temperatures.

3.2. Abnormal superfluid fraction of electrons: dependence on temperature

Let us begin our investigation of interacting electrons by studying the two-particle Hamiltonian. The relative and center of mass coordinates are separable; the center-of-mass energy spectrum is solved analytically and the relative energy spectrum is obtained by the finite-element method. Eigen energies subject to a relative energy cutoff of around $100\hbar\Omega$ are computed. We calculate the actual moment of inertia I through $I = \hbar^2 \langle M^2 \rangle_{th}/(k_B T)$, where M is the angular momentum projection quantum number and $\langle \rangle$ indicates the thermal average [49]. The classical moment of inertia I_{cl} is obtained from the thermal average $\left\langle \sum_{k=1}^{N} r_{k,\perp}^2 \right\rangle$. Here $r_{k,\perp}^2$ is the square of distance of the kth particle to the z axis. Due to spherical symmetry, it is related to the trap energy $\left\langle \sum_{k=1}^{N} r_{k,\perp}^2 \right\rangle_{th} = \frac{4}{3} \left\langle \sum_{k=1}^{N} \frac{1}{2} r_k^2 \right\rangle_{th}$ where the trap energy is then evaluated by converting it to the thermal average of the derivative of the energy with respect to the trap depth through the Hellmann–Feynman theorem. The solid blue, dotted red, and dashed green lines in figure 3 show the numerical results for $\lambda = 0$, $\lambda = 1$, and $\lambda = 10$. First and foremost, we note that these results are in excellent agreement to our new PIMC results, which are depicted by the corresponding symbols. Secondly, we find that the coupling strength has a comparatively small impact on the behaviour of γ_{sf} even for $\lambda = 10$; indeed, the results for moderate coupling ($\lambda = 1$) can hardly be distinguished from the ideal curve. This is a strong indication that the response of electrons in a quantum dot to an external rotation is largely determined by the properties of the corresponding noninteracting system.

Let us next consider our new PIMC data for the temperature dependence of γ_{sf} for larger systems that is shown in figure 4. The left panel shows results for $N = 4$ particles, and the squares and circles have been obtained for Fermi- and Bose-statistics. The green curves show results for the ideal case ($\lambda = 0$) already discussed in figure 2 above and have been included as a reference. The dash-double-dotted grey curves have been obtained for a small yet finite value of the coupling parameter, $\lambda = 0.5$, and closely follow the ideal
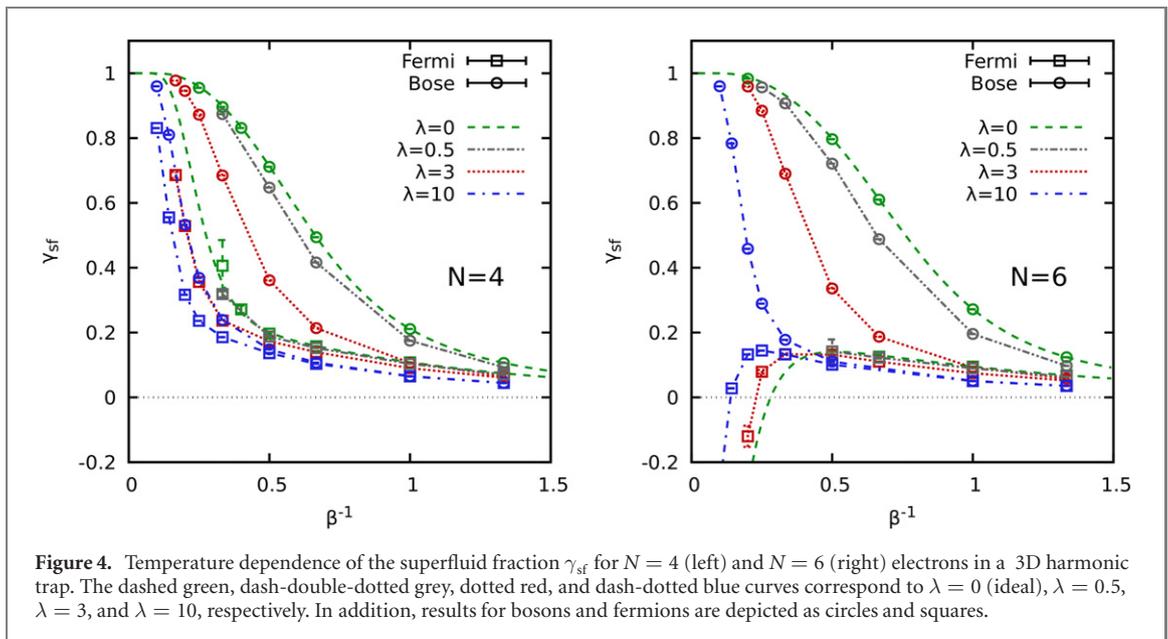
Figure 4. Temperature dependence of the superfluid fraction γ_{sf} for $N = 4$ (left) and $N = 6$ (right) electrons in a 3D harmonic trap. The dashed green, dash-double-dotted grey, dotted red, and dash-dotted blue curves correspond to $\lambda = 0$ (ideal), $\lambda = 0.5$, $\lambda = 3$, and $\lambda = 10$, respectively. In addition, results for bosons and fermions are depicted as circles and squares.

case. In particular, the fermionic results cannot be distinguished from the noninteracting curve with the bare eye, whereas the gap for Bose-statistics is significant.
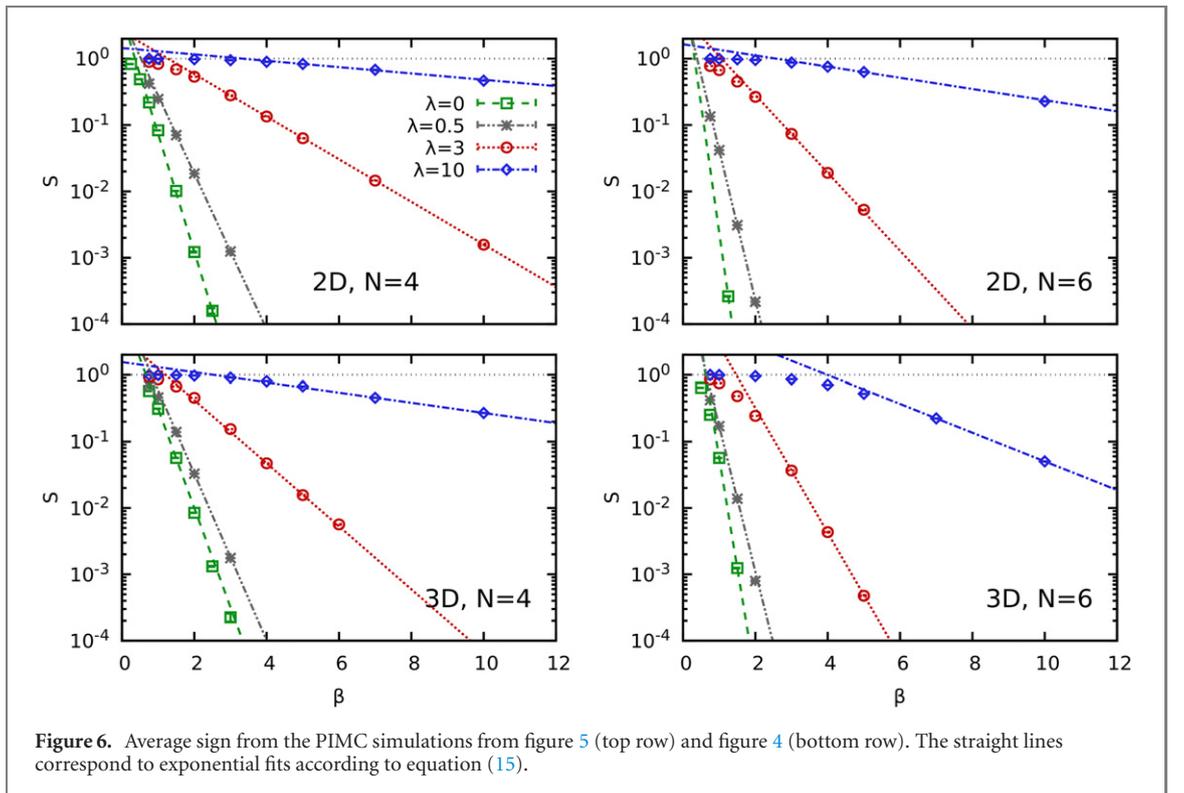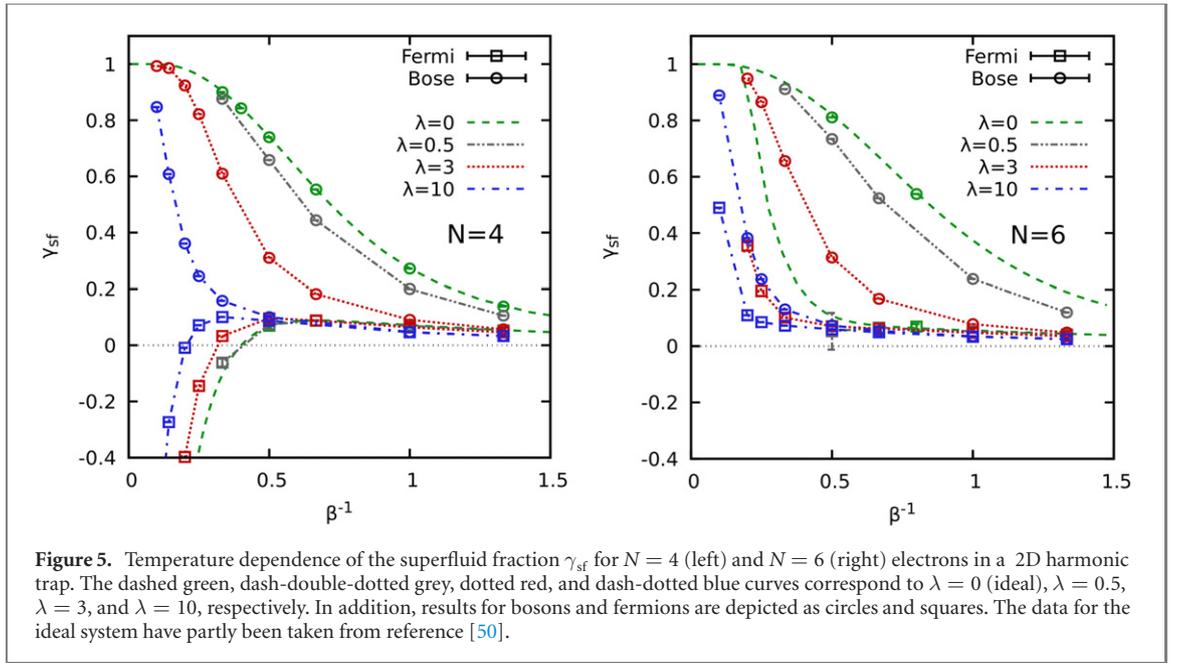
Going to moderate coupling strength, $\lambda = 3$ (dashed red), shifts the curves substantially to the left compared to smaller λ. Heuristically, this can be understood as follows: due to the stronger Coulomb repulsion, the particles are more clearly separated. Consequently, it takes lower temperatures until paths of different particles overlap, which is the driving mechanism of a large superfluid fraction [48, 52]. Again, we find that the effect of the Coulomb repulsion is more pronounced in the case of bosons compared to fermions. The reason for this effect has been reported by Dornheim [50] for the case of dipole–dipole interaction: for fermions, weak interactions are effectively masked by the Pauli exclusion principle which separates even ideal fermions from each other; in contrast, bosons tend to cluster next to each other, and are thus more strongly affected by the Coulomb repulsion. A more detailed analysis of this effect is presented in section 3.4 below.

Finally, the blue curves correspond to relatively strong coupling, $\lambda = 10$. Interestingly, the curves for the two different types of quantum statistics are quite close to each other in this case, and both approach unity for similar temperatures.

Let us next consider the same property, but for $N = 6$ shown in the right panel of figure 4. For bosons, we find a quite similar picture compared to the left panel. Evidently, the particular particle number does not substantially shape the qualitative physical behaviour at these conditions. In stark contrast, all fermionic curves attain a maximum in γ_{sf} in the range $0.5 \leqslant \beta \leqslant 5$ until they diverge towards negative infinity for $T \to 0$. Still, the impact of the coupling parameter λ is only quantitative, and the main feature is already present in the ideal case. Furthermore, we again find that fermions are less affected by the Coulomb repulsion compared to bosons.

In figure 5, we present a similar analysis, but for a purely 2D system. The results are very similar to the 3D case, but the $T = 0$ limit is flipped in the case of fermions: for $N = 4$, γ_{sf} diverges towards negative infinity, and for $N = 6$, it attains unity just as in the Bose-case. Still, the phenomenological reason is the same for both 2D and 3D: it is the presence of a state with finite circulation [49] in the respective cases that causes the negative divergence of the superfluid fraction.

Let us briefly postpone our analysis of the connection of the abnormal superfluid fraction of fermions to the structural properties of the system to touch upon the manifestation of the FSP. In figure 6, we show the PIMC expectation values for the denominator in equation (4), i.e., the average sign. The top and bottom rows have been obtained for 2D and 3D systems, and the left and right columns correspond to $N = 4$ and $N = 6$ spin-polarized electrons. Furthermore, the different data points distinguish data for various values of the coupling parameter λ. First and foremost, we note that all depicted curves exhibit the same qualitative behaviour: for small β (large temperatures), the extension of the paths of different particles is substantially smaller than the average inter-particle separation. Consequently, permutation cycles only rarely appear in the PIMC simulation, most configuration weights are positive, and the average sign is large. With decreasing temperature, the thermal wavelength increases as $\lambda_\beta \sim \sqrt{\beta}$ and, eventually, the paths of all particles in the system overlap. This makes the formation of permutation cycles significantly more likely, configurations

Figure 5. Temperature dependence of the superfluid fraction γ_{sf} for $N = 4$ (left) and $N = 6$ (right) electrons in a 2D harmonic trap. The dashed green, dash-double-dotted grey, dotted red, and dash-dotted blue curves correspond to $\lambda = 0$ (ideal), $\lambda = 0.5$, $\lambda = 3$, and $\lambda = 10$, respectively. In addition, results for bosons and fermions are depicted as circles and squares. The data for the ideal system have partly been taken from reference [50].

Figure 6. Average sign from the PIMC simulations from figure 5 (top row) and figure 4 (bottom row). The straight lines correspond to exponential fits according to equation (15).
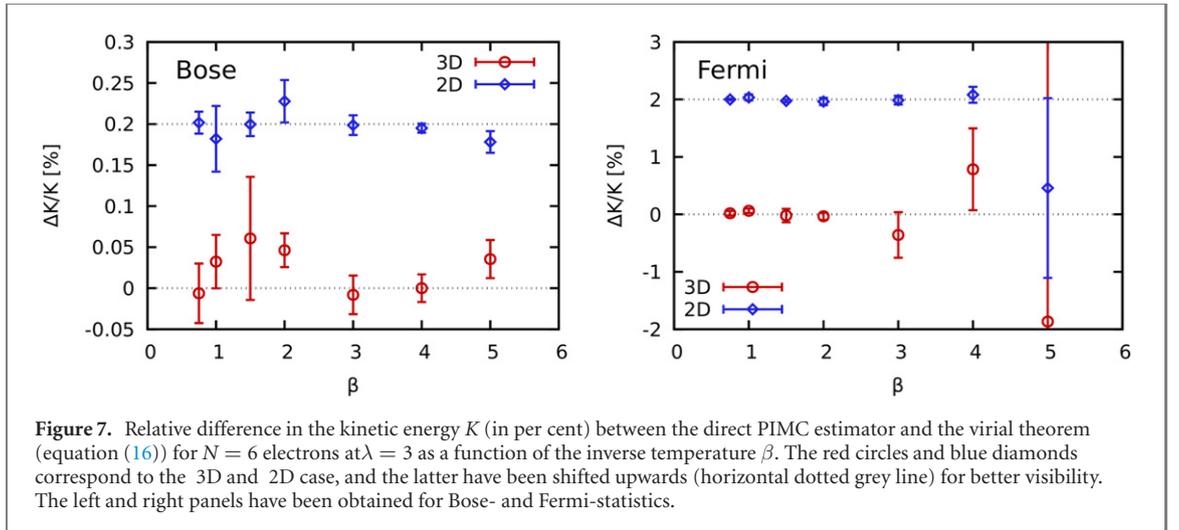
with positive and negative weights appear with a similar frequency in the PIMC simulation, and the average sign drops. The straight lines in figure 6 have been obtained from exponential fits according to

$$S(\beta) = a\,e^{-b\beta} \tag{15}$$

above an empirical minimum value of β, with a and b being the free parameters. Evidently, the fits are in excellent agreement to the PIMC data, which confirms the exponential nature of the FSP reported in earlier studies [45].

A related interesting point is the PIMC estimation of the corresponding energies. More specifically, we consider the well-known virial theorem [69], which gives a relation between the kinetic (K), interaction
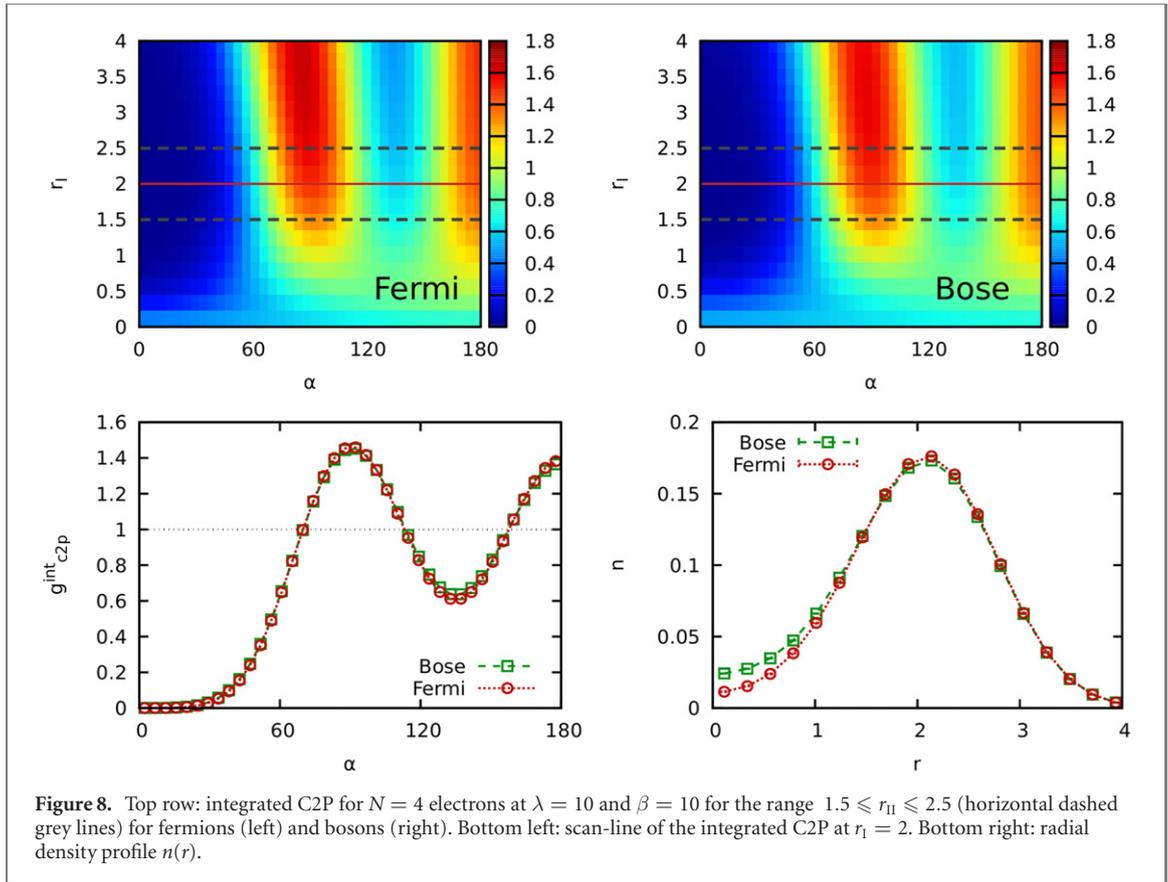
Figure 7. Relative difference in the kinetic energy K (in per cent) between the direct PIMC estimator and the virial theorem (equation (16)) for $N = 6$ electrons at $\lambda = 3$ as a function of the inverse temperature β. The red circles and blue diamonds correspond to the 3D and 2D case, and the latter have been shifted upwards (horizontal dotted grey line) for better visibility. The left and right panels have been obtained for Bose- and Fermi-statistics.

(W), and external potential (v_{ext}) contributions to the total energy,

$$K = V_{ext} - \frac{W}{2}. \tag{16}$$

In practice, we directly estimate K in our PIMC simulation using the standard thermodynamic estimator (see, e.g., reference [40]) and compare it to the right-hand side of equation (16). The results are depicted in figure 7, where we show the relative deviation between the two estimations of K in per cent. We note that the virial theorem as it is given in equation (16) is a general property of the Hamiltonian and holds independent of the particular type of quantum statistics. The left panel has been obtained for Bose-statistics, and the red circles and blue diamonds show results for the 3D and 2D case, where the latter have been shifted by 0.2% for better visibility. Evidently, all data points fluctuate around zero deviation within the given level of statistical uncertainty. Further, we find that the error bars are only weakly dependent on β, and are of the order of $\Delta K/K \sim 0.01\%$.

The right panels shows results from the same simulation computed for Fermi-statistics by evaluating equation (4). Again, we find that the data points fluctuate around zero deviation between the two different estimations of K, which is a strong verification of our simulation scheme and its implementation. Yet, we find a drastic increase of the error bars with β as predicted by equation (6). This nicely illustrates the relative difficulty of fermionic PIMC simulations compared to the Bose-case, where this problem is absent. In particular, simulations of as few as four electrons become unfeasible even on modern supercomputers when the temperature is decreased.
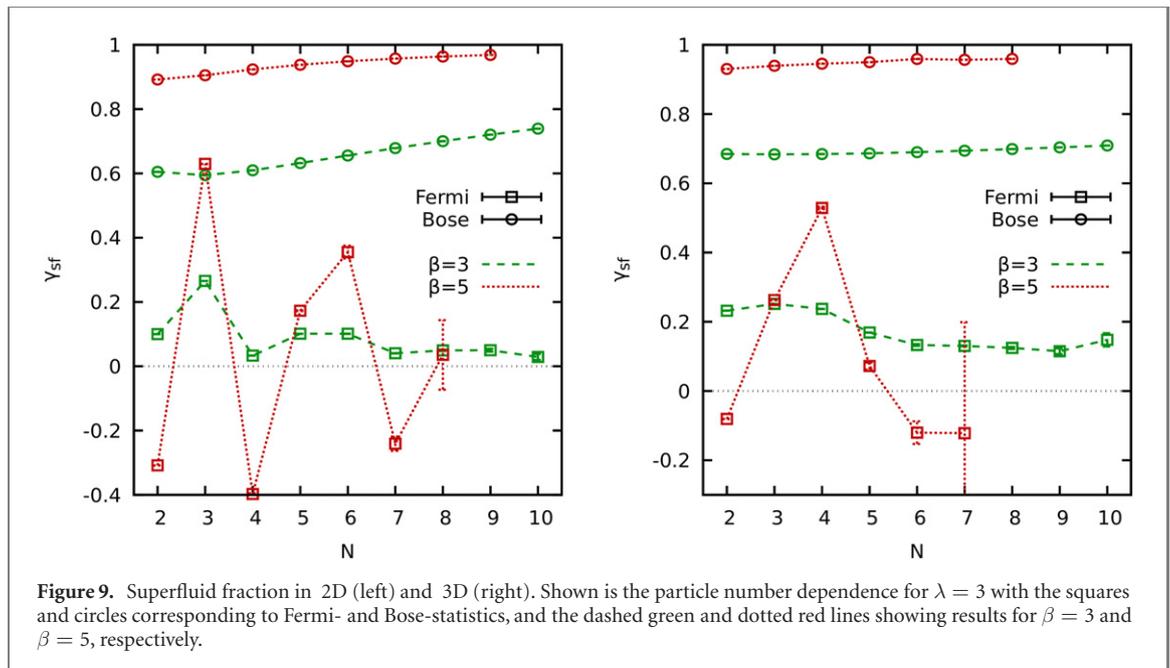
Let us next consider the structural properties of electrons in a 2D quantum dot, and their relation to the abnormal superfluid fraction reported above. To this end, we estimate the integrated C2P defined in equation (13) in section 2.4. The results are shown in figure 8 for $N = 4$ at $\lambda = 10$ and $\beta = 10$. The top row shows the integrated C2P itself in the $\alpha - r_I$-plane, with the reference particle being located somewhere in the range $1.5 \leqslant r_{II} \leqslant 2.5$ (horizontal dashed grey lines), i.e., around the maximum of the radial density (see the bottom right panel of figure 8). Further, the left and right panels show results for fermions and bosons, respectively. Naturally, the C2P is fully symmetric in α around 180 degrees and we restrict ourselves to this half-range. Most importantly, we find that the type of quantum statistics has only very mild effects on the structural properties on the system at these conditions. This is a direct consequence of the strong coupling strength, which effectively separates the paths of individual particles from each other in the PIMC simulation and suppresses the formation of permutation cycles [41]. For small angular separations α, the integrated C2P exhibits a pronounced exchange–correlation hole, followed by a maximum at $\alpha = 90$, a subsequent minimum which is substantially less pronounced than the exchange–correlation hole itself, and a second maximum at the opposite end of the system, i.e., around $\alpha = 180$. This can be seen particularly well in the bottom left panel of figure 8, where we show a scan-line over the C2P at $r_I = 2$, see the solid red line in the top row. The red circles and green squares show results for fermions and bosons, but the deviations between the two data sets can barely be resolved with the naked eye. From a physical perspective, this indicates that the most common configuration of particles is given by a single ring around the center of the trap containing all four particles. This is further substantiated by the radial density profile $n(r)$ shown in the bottom right panel of figure 8. Here the main impact of quantum statistics can be found around $r = 0$, where the probability to find a fermionic particle is reduced compared to the case of bosons.

Figure 8. Top row: integrated C2P for $N = 4$ electrons at $\lambda = 10$ and $\beta = 10$ for the range $1.5 \leqslant r_{II} \leqslant 2.5$ (horizontal dashed grey lines) for fermions (left) and bosons (right). Bottom left: scan-line of the integrated C2P at $r_I = 2$. Bottom right: radial density profile $n(r)$.

Let us now connect these findings regarding the structural properties of the system to the abnormal superfluid fraction investigated above. In particular, it can be seen in figure 5 that γ_{sf} strongly depends on the type of quantum statistics at these conditions. Remarkably, this is not reflected in the structural properties of the system, which, indeed, can hardly be distinguished at all. From a practical perspective, this nontrivial observation can be directly traced back to the estimation of NCRI in the path-integral picture via the area estimator equation (9). In a configuration without any pair exchange, substantial parts of the contributions to the full area **A** (equation (10)) for each configuration are expected to cancel, as, on average, area contributions with positive and negative orientation are equally likely. This only significantly changes upon the formation of permutation cycles, for which all particles contribute with the same orientation to equation (10). The negative superfluid fraction in the case of fermions, therefore, is due to the contribution of configurations with (a) one pair exchange (i.e., a single permutation cycle containing two particles and two individual particle paths) or (b) three pair exchanges (i.e., a single permutation cycle containing all $N = 4$ particles); these are the only two possibilities that contribute with a negative weight to the expectation value of $\langle A_z^2 \rangle$ when being evaluated as the fermionic ratio in equation (4). For bosons, all contributions remain positive. The PIMC-based estimation of the structural properties, on the other hand, is much less, and much more indirectly affected by the permutation structure of a configuration. In particular, structural properties are to a large degree determined by configurations without any permutations in it (we find an average sign of $S = 0.47$ for these conditions, indicating that exchange effects are not a dominant aspect of the system [45]) as no inherent cancellation as in the area estimator takes place. The only cancellation is due to sign changes for different permutation cycles, but this effect is comparably small here. For completeness, we note that, for very large λ, the formation of permutation cycles in our PIMC simulations will be prevented by the strong Coulomb repulsion; in this case, we expect to see no difference between bosons and fermions for either the structural properties or for the quantum moment of inertia.

3.3. Particle number dependence

A further interesting topic of investigation is the dependence of the properties of small electronic systems on the number of particles. In this context, we mention that the properties of confined few-particle systems often sensitively depend on N, which can be seen particularly well in the investigation of addition energies [22–25]. Furthermore, Filinov *et al* [52] have found that the NCRI of strongly coupled charged bosons

Figure 9. Superfluid fraction in 2D (left) and 3D (right). Shown is the particle number dependence for $\lambda = 3$ with the squares and circles corresponding to Fermi- and Bose-statistics, and the dashed green and dotted red lines showing results for $\beta = 3$ and $\beta = 5$, respectively.

exhibits certain 'magic numbers', where the superfluid fraction is most pronounced. In this work, we provide a similar analysis for the superfluid fraction γ_{sf} of electrons in quantum dots.

The results are shown in figure 9, where we show the N-dependence of γ_{sf} both in 2D (left panel) and 3D (right panel) at moderate coupling, $\lambda = 3$. The circles and squares show results for Bose- and Fermi-statistics, and the red and green curves have been obtained for $\beta = 5$ and $\beta = 3$. For all depicted cases, the bosonic curves are quite smooth and exhibit a monotonous increase (the small exception being $N = 3$ for $\beta = 3$ in 2D) in the superfluid fraction with N. Heuristically, this can be understood as follows: in the harmonic trap, the average density increases with N. This, in turn, leads to an increased value of the degeneracy parameter $\chi = \lambda_\beta/\overline{r}$, where $\overline{r}$ is the average inter-particle distance [48], and thus to an increasing value of γ_{sf}.
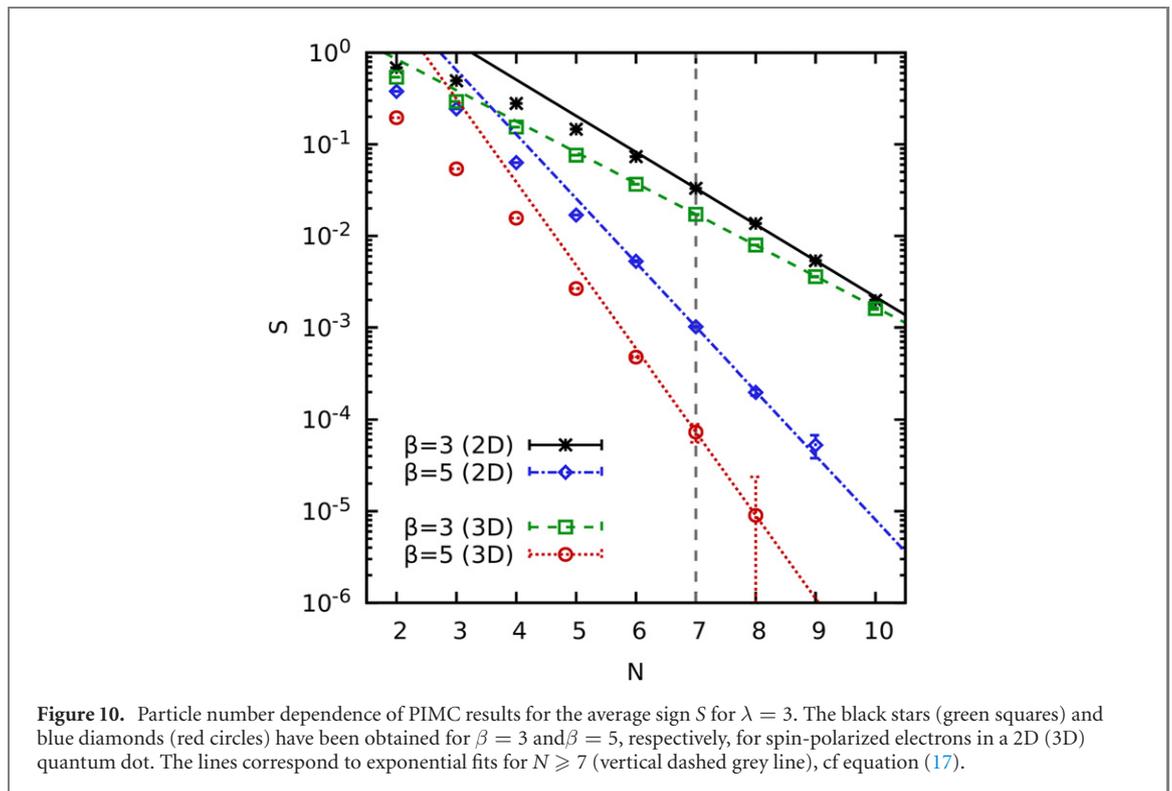
For fermions, on the other hand, the situation is significantly more complicated and interesting. In the 2D-case, the superfluid fraction is rapidly oscillating with N, which is especially pronounced for $\beta = 5$. In particular, the negative and positive values of γ_{sf} can be traced back to the ideal case, see reference [50] for such data in two dimensions. A second trend, which can be seen most clearly for $\beta = 3$, is given by the overall decrease of the superfluid fraction with N. This, too, is expected by simple physical intuition. An increase in N leads to a transition from a finite to a bulk system. For bosons, the crossover from a normal to a superfluid system then attains the character of a true phase transition under the right conditions [48]. In contrast, a single species of fermions such as spin-polarized electrons cannot exhibit the required off-diagonal long-range order [63], and a corresponding bulk system will thus not be superfluid. This is reflected in the observed decrease in γ_{sf} with N. For completeness, we mention that superfluidity in Fermi-systems is still possible, but requires a pairing mechanism such as the interaction with phonons leading to superconductivity [70].

We find similar trends in the case of fermions for 3D systems, although both the oscillations with N and the decrease with increasing system size are somewhat less pronounced.

Let us conclude this investigation of the N-dependence by briefly revisiting the FSP. To this end, we show the average sign obtained for the simulations shown in figure 9 in figure 10. The points show the PIMC data, and the straight lines correspond to exponential fits of the form

$$S(N) = a\,e^{-bN}, \tag{17}$$

and have been obtained by introducing an empirical minimum value of $N = 7$ (vertical dashed grey line). Strictly speaking, equation (17) is only expected to hold for a bulk system such as the uniform electron gas [10, 45], whereas the dependence of a finite, trapped system is expected to be more complicated. Still, we do find at least a qualitative agreement with the exponential decay. The particularly small value of S for the 3D case at $\beta = 5$ is directly reflected by the large error bars in γ_{sf} observed in figure 9. This again strongly illustrates the severe limitations of fermionic PIMC simulations due to the notorious sign problem.

Figure 10. Particle number dependence of PIMC results for the average sign S for $\lambda = 3$. The black stars (green squares) and blue diamonds (red circles) have been obtained for $\beta = 3$ and $\beta = 5$, respectively, for spin-polarized electrons in a 2D (3D) quantum dot. The lines correspond to exponential fits for $N \geqslant 7$ (vertical dashed grey line), cf equation (17).

3.4. Dependence on coupling strength

A highly interesting question is the precise nature of the intricate interplay of the Coulomb repulsion with the effect of quantum statistics. In this regard, our computationally expensive PIMC simulations are uniquely suited to provide reliable answers as no approximations are involved. In figure 11, we show results for the integrated C2P (cf equation (13) above) for $N = 4$ spin-polarized electrons in a 2D harmonic trap at a moderate temperature, $\beta = 1$. The left and right columns have been obtained for Fermi- and Bose-statistics, and the reference particle is always located in the interval $1.5 \leqslant r_{\text{II}} \leqslant 2.5$ (horizontal dashed grey lines in the top left panel).
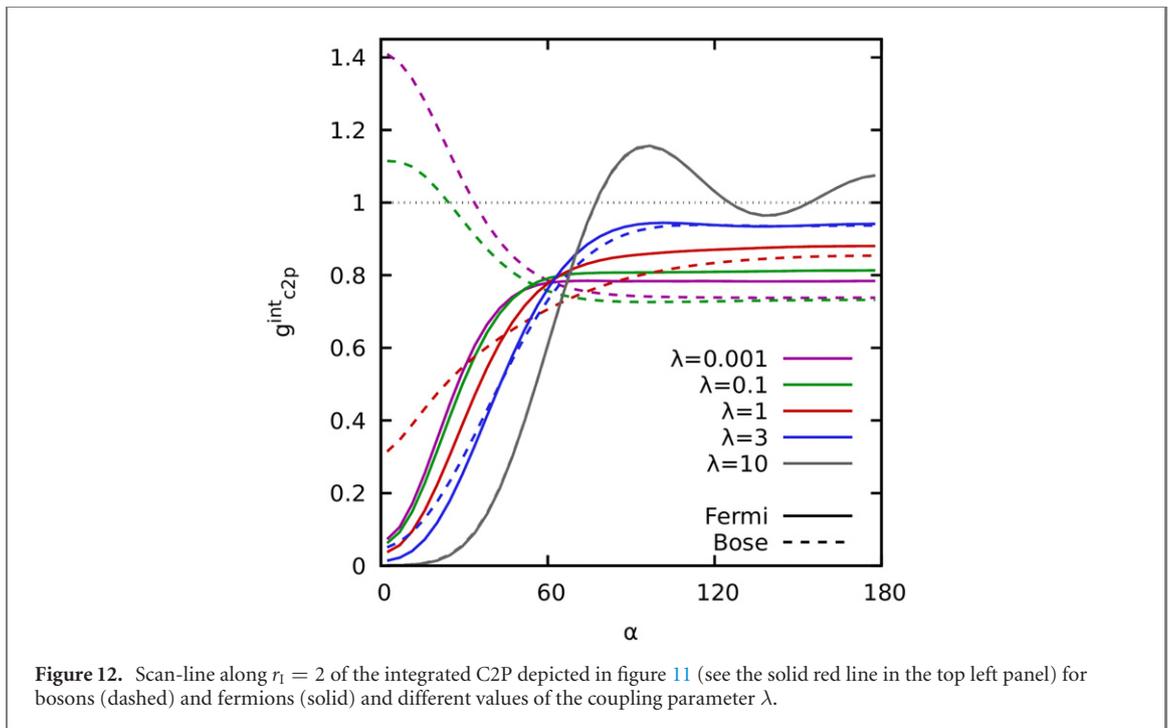
The top row corresponds to a very weakly coupled system $(\lambda = 10^{-3})$, where the Coulomb repulsion has a negligible effect. For fermions, the Pauli exclusion principle nevertheless results in a pronounced exchange–correlation hole around $\alpha = 0$, whereas the rest of the system appears to be relatively featureless. In stark contrast, a corresponding Bose-system at the same conditions exhibits the opposite behaviour, as bosons tend to cluster around each other. Increasing the coupling strength to $\lambda = 0.1$ leaves the Fermi-system unchanged, whereas the positive *exchange–correlation hill* of the bosons is substantially decreased. From a physical perspective, this means that bosons are strongly influenced even by weak repulsive interactions, whereas the latter are effectively masked by the Pauli principle in the case of fermions. For completeness, we mention that the same point has recently been reported by Dornheim [50] in the case of dipole–dipole repulsion. The same trend has also been noted in our discussion of figures 5 and 4 above, where the superfluid fraction γ_{sf} was substantially more affected by the coupling parameter λ for bosons compared to fermions.

Going back to the integrated C2P shown in figure 11, a further increase of the coupling strength to $\lambda = 1$ (middle row) again only leads to very mild changes for Fermi-statistics, whereas there appears a qualitative change for bosons: the exchange–correlation *hill* is changed to a *hole*, although it is still significantly less pronounced compared to the left panel. At $\lambda = 3$, i.e., at moderate coupling, the importance of quantum statistics is drastically reduced and both panels give a nearly identical picture. Finally, the strong Coulomb repulsion at $\lambda = 10$ effectively separates individual particles, and no differences between bosons and fermions can be seen with the naked eye.

Let us next consider figure 12, where we show a scan-line of the integrated C2P at $r_{\text{I}} = 2$ (solid red line in the top left panel of figure 11). The solid and dashed lines distinguish fermions and bosons, and the different colours correspond to values of the coupling parameter λ. The arguably most striking feature of this plot is the *exchange–correlation hill* for bosons at $\lambda \leqslant 0.1$. In addition, it clearly illustrates the small impact of the coupling strength on fermions for the same λ. For $\lambda = 3$, there is still a distinct impact of quantum statistics, whereas no such difference can be resolved for $\lambda = 10$. The latter case also constitutes
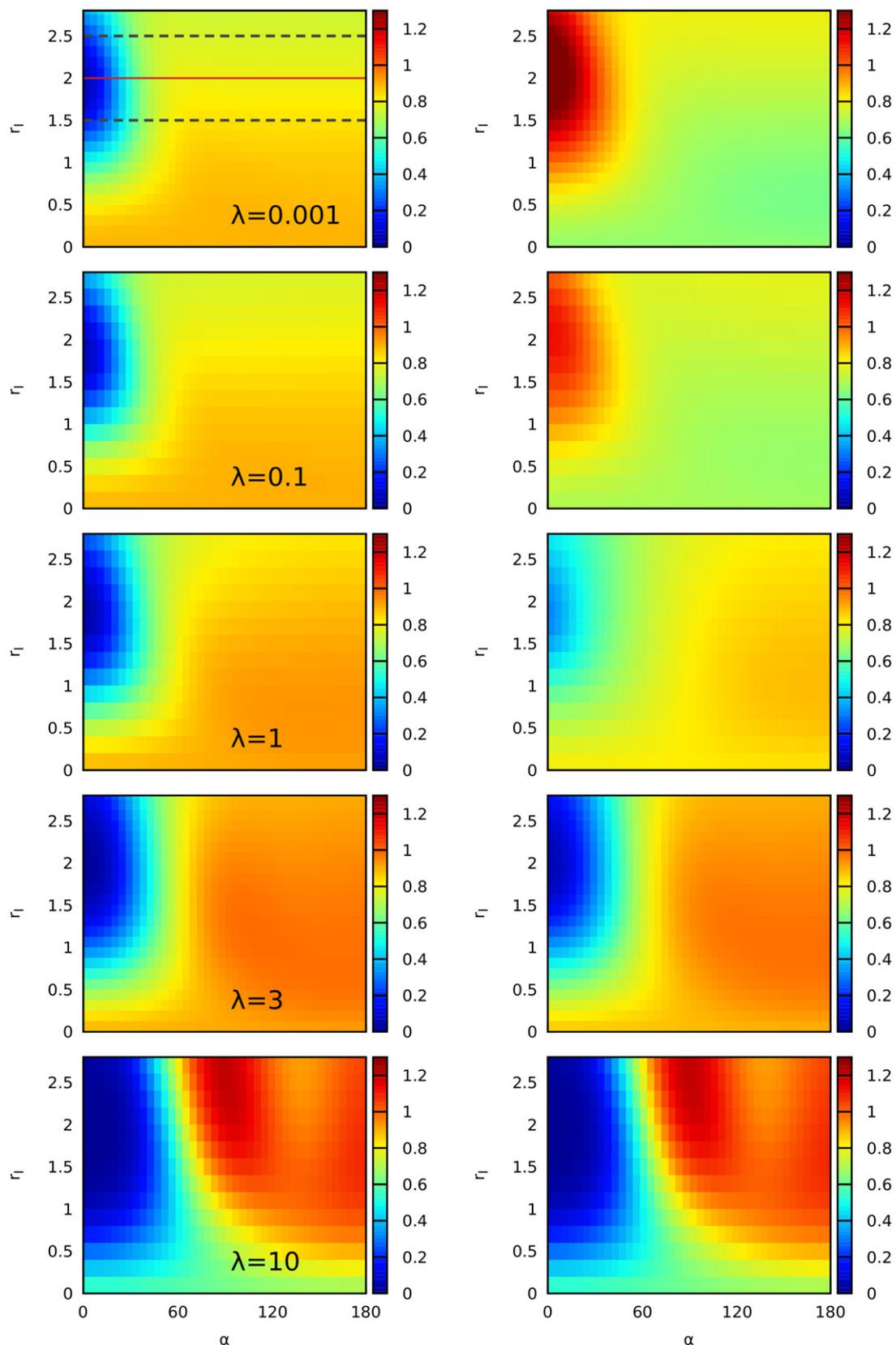
Figure 11. Integrated C2P for $N = 4$ spin-polarized electrons in a harmonic confinement for $\beta = 1$ in 2D for Fermi- (left) and Bose-statistics (right).

Figure 12. Scan-line along $r_{\rm I} = 2$ of the integrated C2P depicted in figure 11 (see the solid red line in the top left panel) for bosons (dashed) and fermions (solid) and different values of the coupling parameter λ.

the only curve with a second maximum around $\alpha = 180$. Let us close this discussion of the integrated C2P with a practical remark. Obviously, the probability to find two identical fermions at the exact same position must always be zero, $\rho_2(r, r, 0) = 0$. Yet, by integrating over a finite range of the reference particle $r_{\rm II,min} \leqslant r_{\rm II} \leqslant r_{\rm II,max}$, the integrated C2P can be nonzero for all values of $r_{\rm I}$ even for $\alpha = 0$.

4. Summary and outlook

In summary, we have presented extensive new *ab initio* PIMC simulation results for electrons in 2D and 3D quantum dots. In particular, we have investigated the NCRI of such systems and have found a divergent, negative abnormal superfluid fraction which manifests under certain conditions due to the interplay of Fermi-statistics and the harmonic confinement [49]. In addition, we have thoroughly investigated the structural properties of such systems by computing the C2P correlation function suggested by Thomsen and Bonitz [51]. The comparison of results for Bose- and Fermi-statistics has revealed that the onset of the abnormal superfluid fraction is hardly connected to the static structure, which can be nearly independent of the type of quantum statistics, whereas the respective superfluid fractions diverge. Within the path-integral picture, this nontrivial finding can be directly explained by the impact of the permutation structure, which strongly affects the area estimator for $\gamma_{\rm sf}$, but only has a small effect on other observables when the average sign S is large. Indeed, the observed divergence of the quantum moment of inertia between bosons and fermions is a direct consequence of the structure of the density matrix with respect to the angular momentum. In addition, we have substantiated earlier findings for harmonically confined quantum dipole systems [50], where it has been found that the repulsion between two fermions is effectively masked by the Pauli exclusion principle for weak too moderate values of the coupling parameter λ. In stark contrast, bosons sensitively react even to small changes in the coupling strength.

We believe that our work has important implications for future work. First and foremost, we note that electrons in a harmonic oscillator potential constitute a very important model system. Our extensive set of exact PIMC results is freely available online [46], and constitutes an unassailable benchmark for the development of new methods and approximations. Moreover, the observed interplay between quantum effects and Coulomb coupling is interesting in its own right and further advances our fundamental understanding of trapped few-body systems. Finally, we note that our predictions for the abnormal quantum moment of inertia can be verified in future experiments in different ways. In principle, it would be sufficient to measure the response of a quantum dot to an external rotation. A more convenient route might be given by the application of an external magnetic field. Indeed, a constant rotation along the z-axis $\vec{\Omega}$ is equivalent to a homogeneous magnetic field along z-axis $B = \frac{-2mc}{e}\vec{\Omega}$. The quantum moment of inertia is proportional to the magnetization vector $\vec{M} = -\vec{H} + \vec{B}/\mu_0$ under an infinitesimal magnetic field B. In this regard, we note that the direct PIMC simulation of electrons in the presence of a finite magnetic

field [71] is likely challenging due to an additional phase problem, and constitutes an important direction for future works.

Additional future extensions of our work might include the investigation of spin-unpolarized systems, which would allow for the study of a spin-resolved C2P. In particular, it is clear that the observed effective screening of the pair interaction by the Pauli principle will not apply to fermions of a different spin-orientation, which will lead to an interesting mixture of different effects. In addition, we note that the central computational bottleneck of the present study is given by the FSP, which precludes the simulation of larger systems and lower temperatures. In this regard, we mention the remarkable recent progress in the fermionic quantum Monte Carlo simulation at finite temperature in the context of warm dense matter research [30, 72–83]. Specifically, the adaption of these novel methods to the simulation of electrons in quantum dots seems promising and rewarding. Finally, we mention that the C2P that has been used in the present work allows to reliably describe crossovers and melting phenomena in finite systems [51]. This is in stark contrast to previously employed Lindemann-type approaches [84] that rely on the underlying Monte Carlo sampling scheme. Thus, the present set-up can be straightforwardly used to study the impact of quantum effects onto the crystallization of trapped few-body systems.

Acknowledgments

Data availability statement

The data that support the findings of this study are openly available at the following URL/DOI: https://doi.org/10.14278/rodare.1931.

ORCID iDs

Tobias Dornheim ⓘ https://orcid.org/0000-0001-7293-6615

References

[1] Ceperley D M 1992 Path-integral calculations of normal liquid ^{3}He *Phys. Rev. Lett.* **69** 331–4

[2] Sköld K, Pelizzari C A, Mason R, Mitchell E W J and White J W 1980 Elementary excitations in liquid ^{3}He *Phil. Trans. R. Soc.* B **290** 605–16

[3] Godfrin H, Meschke M, Lauter H-J, Sultan S, Böhm H M, Krotscheck E and Panholzer M 2012 Observation of a roton collective mode in a two-dimensional Fermi liquid *Nature* **483** 576–9

[4] Nava M, Galli D E, Moroni S and Vitali E 2013 Dynamic structure factor for ^{3}He in two dimensions *Phys. Rev.* B **87** 144506

[5] Dornheim T, Moldabekov Z A, Vorberger V and Militzer B 2022 Path integral Monte Carlo approach to the structural properties and collective excitations of liquid ^{3}He without fixed nodes *Sci. Rep.* **12** 708

[6] Vollhardt D and Wolfle P 2013 *The Superfluid Phases of Helium 3 Dover Books on Physics Series* (New York: Dover)

[7] Graziani F, Desjarlais M P, Redmer R and Trickey S B (ed) 2014 *Frontiers and Challenges in Warm Dense Matter* (Berlin: Springer)

[8] Fortov V E 2009 Extreme states of matter on earth and in space *Phys. Usp.* **52** 615–47

[9] Bonitz M, Dornheim T, Moldabekov Z A, Zhang S, Hamann P, Kählert H, Filinov A, Ramakrishna K and Vorberger J 2020 *Ab initio* simulation of warm dense matter *Phys. Plasmas* **27** 042710

[10] Dornheim T, Groth S and Bonitz M 2018 The uniform electron gas at warm dense matter conditions *Phys. Rep.* **744** 1–86

[11] Dornheim T, Groth S, Vorberger J and Bonitz M 2018 *Ab initio* path integral Monte Carlo results for the dynamic structure factor of correlated electrons: from the electron liquid to warm dense matter *Phys. Rev. Lett.* **121** 255001

[12] Saumon D, Hubbard W B, Chabrier G and van Horn H M 1992 The role of the molecular-metallic transition of hydrogen in the evolution of jupiter, saturn, and brown dwarfs *Astrophys. J.* **391** 827–31

[13] Becker A, Lorenzen W, Fortney J J, Nettelmann N, Schöttler M and Redmer R 2014 *Ab initio* equations of state for hydrogen (h-reos.3) and helium (he-reos.3) and their implications for the interior of brown dwarfs *Astrophys. J. Suppl. Ser.* **215** 21

[14] Militzer B, Hubbard W B, Vorberger J, Tamblyn I and Bonev S A 2008 A massive core in jupiter predicted from first-principles simulations *Astrophys. J.* **688** L45–8

[15] Schöttler M and Redmer R 2018 *Ab initio* calculation of the miscibility diagram for hydrogen-helium mixtures *Phys. Rev. Lett.* **120** 115703

[16] Hu S X, Militzer B, Goncharov V N and Skupsky S 2011 First-principles equation-of-state table of deuterium for inertial confinement fusion applications *Phys. Rev.* B **84** 224109

[17] Reimann S M and Manninen M 2002 Electronic structure of quantum dots *Rev. Mod. Phys.* **74** 1283–342

[18] McDonald C R, Orlando G, Abraham J W, Hochstuhl D, Bonitz M and Brabec T 2013 Theory of the quantum breathing mode in harmonic traps and its use as a diagnostic tool *Phys. Rev. Lett.* **111** 256801

[19] Abraham J W and Bonitz M 2014 Quantum breathing mode of trapped particles: from nanoplasmas to ultracold gases *Contrib. Plasma Phys.* **54** 27–99

[20] Egger R, Häusler W, Mak C H and Grabert H 1999 Crossover from Fermi liquid to Wigner molecule behavior in quantum dots *Phys. Rev. Lett.* **82** 3320–3

[21] Filinov A V, Bonitz M and Lozovik Y E 2001 Wigner crystallization in mesoscopic 2D electron systems *Phys. Rev. Lett.* **86** 3851–4

[22] Harting J, Mülken O and Borrmann P 2000 Interplay between shell effects and electron correlations in quantum dots *Phys. Rev.* B **62** 10207–11

[23] Rontani M, Rossi F, Manghi F and Molinari E 1998 Addition energies in semiconductor quantum dots: role of electron–electron interaction *Appl. Phys. Lett.* **72** 957–9

[24] Schreiber M, Siewert J and Vojta T 2001 Interacting electrons in parabolic quantum dots: energy levels, addition energies, and charge distributions *Int. J. Mod. Phys.* B **15** 3641–5

[25] Tarucha S, Austing D G, Honda T, van der Hage R J and Kouwenhoven L P 1996 Shell filling and spin effects in a few electron quantum dot *Phys. Rev. Lett.* **77** 3613–6

[26] Tavernier M B, Anisimovas E and Peeters F M 2004 Correlation between electrons and vortices in quantum dots *Phys. Rev.* B **70** 155321

[27] Tavernier M B, Anisimovas E and Peeters F M 2006 Ground state and vortex structure of the $n = 5$ and $n = 6$ electron quantum dot *Phys. Rev.* B **74** 125305

[28] Li Y, Yannouleas C and Landman U 2006 From a few to many electrons in quantum dots under strong magnetic fields: properties of rotating electron molecules with multiple rings *Phys. Rev.* B **73** 075301

[29] Blume D 2012 Few-body physics with ultracold atomic and molecular systems in traps *Rep. Prog. Phys.* **75** 046401

[30] Dornheim T, Groth S, Filinov A and Bonitz M 2015 Permutation blocking path integral Monte Carlo: a highly efficient approach to the simulation of strongly degenerate non-ideal fermions *New J. Phys.* **17** 073017

[31] Egger R and Mak C H 2001 Multilevel blocking Monte Carlo simulations for quantum dots *Int. J. Mod. Phys.* B **15** 1416–25

[32] Schoof T, Bonitz M, Filinov A, Hochstuhl D and Dufty J W 2011 Configuration path integral Monte Carlo *Contrib. Plasma Phys.* **51** 687–97

[33] Hirshberg B, Invernizzi M and Parrinello M 2020 Path integral molecular dynamics for fermions: alleviating the sign problem with the Bogoliubov inequality *J. Chem. Phys.* **152** 171102

[34] Dornheim T, Invernizzi M, Vorberger J and Hirshberg B 2020 Attenuating the fermion sign problem in path integral Monte Carlo simulations using the Bogoliubov inequality and thermodynamic integration *J. Chem. Phys.* **153** 234104

[35] Dornheim T 2021 Fermion sign problem in path integral Monte Carlo simulations: grand-canonical ensemble *J. Phys. A: Math. Theor.* **54** 335001

[36] Dornheim T, Groth S and Bonitz M 2019 Permutation blocking path integral Monte Carlo simulations of degenerate electrons at finite temperature *Contrib. Plasma Phys.* **59** e201800157

[37] Voznesenskiy M A, Vorontsov-Velyaminov P N and Lyubartsev A P 2009 Path-integral—expanded-ensemble Monte Carlo method in treatment of the sign problem for fermions *Phys. Rev.* E **80** 066702

[38] Lyubartsev A P 2005 Simulation of excited states and the sign problem in the path integral Monte Carlo method *J. Phys. A: Math. Gen.* **38** 6659–74

[39] Xie H, Null L and Wang L 2022 *Ab initio* study of interacting fermions at finite temperature with neural canonical transformation *J. Mach. Learn.* **1** 38–59

[40] Ceperley D M 1995 Path integrals in the theory of condensed helium *Rev. Mod. Phys.* **67** 279

[41] Dornheim T, Groth S, Filinov A V and Bonitz M 2019 Path integral Monte Carlo simulation of degenerate electrons: permutation-cycle properties *J. Chem. Phys.* **151** 014108

[42] Ceperley D M 1991 Fermion nodes *J. Stat. Phys.* **63** 1237–67

[43] Troyer M and Wiese U J 2005 Computational complexity and fundamental limitations to fermionic quantum Monte Carlo simulations *Phys. Rev. Lett.* **94** 170201

[44] Loh E Y, Gubernatis J E, Scalettar R T, White S R, Scalapino D J and Sugar R L 1990 Sign problem in the numerical simulation of many-electron systems *Phys. Rev.* B **41** 9301–7

[45] Dornheim T 2019 Fermion sign problem in path integral Monte Carlo simulations: quantum dots, ultracold atoms, and warm dense matter *Phys. Rev.* E **100** 023307

[46] Dornheim T 2022 Repository containing all PIMC raw data

[47] Kwon Y and Birgitta Whaley K 1999 Atomic-scale quantum solvation structure in superfluid helium-4 clusters *Phys. Rev. Lett.* **83** 4108–11

[48] Dornheim T, Filinov A and Bonitz M 2015 Superfluidity of strongly correlated bosons in two- and three-dimensional traps *Phys. Rev.* B **91** 054503

[49] Yan Y and Blume D Jun 2014 Abnormal superfluid fraction of harmonically trapped few-fermion systems *Phys. Rev. Lett.* **112** 235301

[50] Dornheim T 2020 Path-integral Monte Carlo simulations of quantum dipole systems in traps: superfluidity, quantum statistics, and structural properties *Phys. Rev.* A **102** 023307

[51] Thomsen H and Bonitz M 2015 Resolving structural transitions in spherical dust clusters *Phys. Rev.* E **91** 043104

[52] Filinov A, Böning J, Bonitz M and Lozovik Y 2008 Controlling the spatial distribution of superfluidity in radially ordered coulomb clusters *Phys. Rev.* B **77** 214527

[53] Herman M F, Bruskin E J and Berne B J 1982 On path integral Monte Carlo simulations *J. Chem. Phys.* **76** 5150–5

[54] Takahashi M and Imada M 1984 Monte Carlo calculation of quantum systems *J. Phys. Soc. Japan* **53** 963–74

[55] De Raedt H and De Raedt B 1983 Applications of the generalized trotter formula *Phys. Rev.* A **28** 3575–80

[56] Brualla L, Sakkos K, Boronat J and Casulleras J 2004 Higher order and infinite trotter-number extrapolations in path integral Monte Carlo *J. Chem. Phys.* **121** 636–43

[57] Mezzacapo F and Boninsegni M 2007 Structure, superfluidity, and quantum melting of hydrogen clusters *Phys. Rev.* A **75** 033201

[58]   Boninsegni M, Prokofev N V and Svistunov B V 2006 Worm algorithm and diagrammatic Monte Carlo: a new approach to continuous-space path integral Monte Carlo simulations *Phys. Rev.* E **74** 036701

[59]   Boninsegni M, Prokofev N V and Svistunov B V 2006 Worm algorithm for continuous-space path integral Monte Carlo simulations *Phys. Rev. Lett.* **96** 070601

[60]   Ceperley D M 1996 Path integral Monte Carlo methods for fermions *Monte Carlo and Molecular Dynamics of Condensed Matter* ed G C K Binder (Bologna: Società Italiana di Fisica)

[61]   Sindzingre P, Ceperley D M and Klein M L 1991 Superfluidity in clusters of p-h_2 molecules *Phys. Rev. Lett.* **67** 1871–4

[62]   Krauth W 2006 *Statistical Mechanics: Algorithms and Computations Oxford Master Series in Physics* (Oxford: Oxford University Press)

[63]   Shi Y 2005 Superfluidity or supersolidity as a consequence of off-diagonal long-range order *Phys. Rev.* B **72** 014533

[64]   Dornheim T, Thomsen H, Ludwig P, Filinov A and Bonitz M 2016 Analyzing quantum correlations made simple *Contrib. Plasma Phys.* **56** 371–9

[65]   Ott T, Thomsen H, Abraham J W, Dornheim T and Bonitz M 2018 Recent progress in the theory and simulation of strongly correlated plasmas: phase transitions, transport, quantum, and magnetic field effects *Eur. Phys. J.* D **72** 84

[66]   Chin S A and Krotscheck E 1995 Systematics of pure and doped ^{4}He clusters *Phys. Rev.* B **52** 10405–28

[67]   Thomsen H 2015 Melting processes and laser manipulation of strongly coupled Yukawa systems PhD Thesis Kiel University

[68]   Zagrebnov V A and Bru J-B 2001 The Bogoliubov model of weakly imperfect Bose gas *Phys. Rep.* **350** 291–434

[69]   Greiner W, Neise L, Stocker H, Stöcker H and Rischke D 1995 Thermodynamics and statistical mechanics *Classical Theoretical Physics* (Berlin: Springer)

[70]   Bardeen J, Cooper L N and Schrieffer J R 1957 Theory of superconductivity *Phys. Rev.* **108** 1175–204

[71]   Tőke C and Galambos T H 2019 Path-integral Monte Carlo study of electronic states in quantum dots in an external magnetic field *Phys. Rev.* B **100** 165136

[72]   Malone F D, Blunt N S, Shepherd J J, Lee D K K, Spencer J S and Foulkes W M C 2015 Interaction picture density matrix quantum Monte Carlo *J. Chem. Phys.* **143** 044116

[73]   Malone F D, Blunt N S, Brown E W, Lee D K K, Spencer J S, Foulkes W M C and Shepherd J J 2016 Accurate exchange–correlation energies for the warm dense electron gas *Phys. Rev. Lett.* **117** 115701

[74]   Dornheim T, Groth S, Schoof T, Hann C and Bonitz M 2016 *Ab initio* quantum Monte Carlo simulations of the uniform electron gas without fixed nodes: the unpolarized case *Phys. Rev.* B **93** 205134

[75]   Dornheim T, Groth S, Sjostrom T, Malone F D, Foulkes W M C and Bonitz M 2016 *Ab initio* quantum Monte Carlo simulation of the warm dense electron gas in the thermodynamic limit *Phys. Rev. Lett.* **117** 156403

[76]   Groth S, Dornheim T, Sjostrom T, Malone F D, Foulkes W M C and Bonitz M 2017 *Ab initio* exchange–correlation free energy of the uniform electron gas at warm dense matter conditions *Phys. Rev. Lett.* **119** 135001

[77]   Brown E W, Clark B K, DuBois J L and Ceperley D M 2013 Path-integral Monte Carlo simulation of the warm dense homogeneous electron gas *Phys. Rev. Lett.* **110** 146405

[78]   Liu Y, Cho M and Rubenstein B 2018 *Ab initio* finite temperature auxiliary field quantum Monte Carlo *J. Chem. Theory Comput.* **14** 4722–32

[79]   Claes J and Clark B K 2017 Finite-temperature properties of strongly correlated systems via variational Monte Carlo *Phys. Rev.* B **95** 205109

[80]   Blunt N S, Rogers T W, Spencer J S and Foulkes W M C 2014 Density-matrix quantum Monte Carlo method *Phys. Rev.* B **89** 245124

[81]   Yilmaz A, Hunger K, Dornheim T, Groth S and Bonitz M 2020 Restricted configuration path integral Monte Carlo *J. Chem. Phys.* **153** 124114

[82]   Lee J, Morales M A and Malone F D 2021 A phaseless auxiliary-field quantum Monte Carlo perspective on the uniform electron gas at finite temperatures: issues, observations, and benchmark study *J. Chem. Phys.* **154** 064109

[83]   Hunger K, Schoof T, Dornheim T, Bonitz M and Filinov A 2021 Momentum distribution function and short-range correlations of the warm dense electron gas: *ab initio* quantum Monte Carlo results *Phys. Rev.* E **103** 053204

[84]   Böning J, Filinov A, Ludwig P, Baumgartner H, Bonitz M and Lozovik Y E 2008 Melting of trapped few-particle systems *Phys. Rev. Lett.* **100** 113401